Ultrafast Absorption Difference Spectra of the Fenna-Matthews-Olson Protein at 19 K: Experiment and Simulations

Daniel R. Buck, Sergei Savikhin, and Walter S. Struve
Ames Laboratory-USDOE and Department of Chemistry, Iowa State University, Ames, Iowa 50010 USA

ABSTRACT We describe simulations of absorption difference spectra in strongly coupled photosynthetic antennas. In the presence of large resonance couplings, distinctive features arise from excited-state absorption transitions between one- and two-exciton levels. We first outline the theory for the heterodimer and for the general *N*-pigment system, and we demonstrate the transition between the strong and weak coupling regimes. The theory is applied to Fenna-Matthews-Olson (FMO) bacteriochlorophyll *a* protein trimers from the green photosynthetic bacterium *Prosthecochloris aestuarii* and then compared with experimental low-temperature absorption difference spectra of FMO trimers from the green bacterium *Chlorobium tepidum*.

INTRODUCTION

The availability of stable femtosecond lasers for studying electronic energy transfers in photosynthetic systems (Chachisvilis et al., 1994; Lin et al., 1994; Savikhin et al., 1994; Bittner et al., 1994) has raised the possibility of ascertaining the role of exciton coherence in antenna processes (van Grondelle, 1984). In the weak coupling regime, the electronic excitations are localized on single pigments (Rahman et al., 1979). For pigments with strongly allowed electric dipole transitions between their ground and fluorescing states, the energy migration in this regime is well described in terms of incoherent Förster hopping governed by dipole-dipole interactions (Förster, 1948; Knox, 1975). In the opposite limit of strong coupling, the electronic excitations are delocalized eigenstates of a supermolecule electronic Hamiltonian that encompasses pigment-pigment couplings (Rahman et al., 1979; Pearlstein and Hemenger, 1978). In this extreme, provided no loss of exciton coherence occurs, electronic energy transfers can be viewed as relaxation (or equilibration) between well-defined exciton components. Such relaxation would cause spatial redistribution of electronic energy, because different exciton components exhibit contrasting admixtures of single-pigment excitations (Pearlstein, 1992).

Our objective is to understand the effects of exciton coherence on the absorption difference spectroscopy of strongly coupled antennas. The second section of this paper deals with the spectroscopy of the strongly coupled heterodimer. It describes the influence of relaxation between its two exciton components on the photobleaching (PB), stimulated emission (SE), and excited-state absorption (ESA) spectra. As in larger antennas with >2 pigments (Lin et al., 1991), the ESA spectrum is influenced by transitions between one-exciton and two-exciton levels, which are necessarily nearly isoenergetic with transitions between the ground and one-exciton levels. The effects of one- to two-exciton transitions on the spectroscopy of linear J-aggregates are already well appreciated (Spano and Mukamel, 1989). Because our theory for absorption difference spectra in strongly coupled antennnas has not been articulated beyond the terse descriptions of Lin et al. (1991) and van Amerongen and Struve (1991), we expand on it in more detail here. We show that in the weak coupling limit, the absorption difference spectroscopy of the strongly coupled heterodimer coincides with that of two noninteracting pigments. We then generalize the theory to arbitrary *N*-pigment systems in the third section. Finally, in the fourth section, we apply the theory to bacteriochlorophyll (BChl) *a* protein antenna complexes (Fenna-Matthews-Olson, or FMO trimers) from green sulfur bacteria (Matthews and Fenna, 1980; Tronrud et al., 1986). The effects of exciton interactions on the absorption difference spectra are illustrated by comparing theoretical spectra observed in the presence and absence of realistic resonance couplings between the BChl *a* pigments in FMO trimers from the green bacterium *Prosthecochloris aestuarii* (Pearlstein, 1992). These results are an extension of earlier simulations of the pump-probe spectroscopy of FMO trimers (van Amerongen and Struve, 1991). Finally, we compare these simulations with recent low-temperature absorption difference spectra for FMO trimers from the green bacterium *Chlorobium tepidum*.

THE HETERODIMER

In this section we consider the absorption difference spectra of two strongly interacting pigments A and B. We denote the electronic ground state of the heterodimer as $|AB\rangle \equiv |00\rangle$. The one-exciton states $|+\rangle$, $|-\rangle$ are linear combinations of the localized excited states $|A^*B\rangle \equiv |10\rangle$ and $|AB^*\rangle \equiv |01\rangle$, in which either pigment A or pigment B is excited; i.e.,

Received for publication 13 August 1996 and in final form 15 October 1996.

Address reprint requests to Dr. Walter S. Struve, Department of Chemistry, Iowa State University, Gilman Hall, Ames, IA 50011-3111. Tel.: 515-294-4276; Fax: 515-294-1699; E-mail: wstruve@ameslab.gov.

0006-3495/97/01/24/13 $2.00

they are the delocalized states

$$|+\rangle = c_1|10\rangle + c_2|01\rangle \quad (1)$$

$$|-\rangle = d_1|10\rangle + d_2|01\rangle.$$

The energies of the delocalized states, obtained by diagonalizing the Hamiltonian matrix

$$H = \begin{bmatrix} E_1 & V \\ V & E_2 \end{bmatrix} \quad (2)$$

are (Landau and Lifschitz, 1958)

$$E_+^{(1)} = \frac{1}{2}(E_1 + E_2) + \frac{\Delta}{2} \quad (3)$$

$$E_-^{(1)} = \frac{1}{2}(E_1 + E_2) - \frac{\Delta}{2}.$$

Here

$$\Delta = \sqrt{(E_1 - E_2)^2 + 4V^2} \quad (4)$$

is the energy splitting between one-exciton levels. E_1 and E_2 would be the excited-state energies of pigments A and B, respectively, in the absence of the resonance interaction ($V = 0$). In the presence of this interaction, the excited-state energies E_1 and E_2 of the isolated pigments become superseded by the exciton levels $E_+^{(1)}$, $E_-^{(1)}$ in Eq. 3. The energy separation Δ between the exciton levels is larger than $|E_1 - E_2|$; i.e., the zeroth-order localized state energies are mutually repelled when the interaction V is turned on. The two pigments are simultaneously excited in the two-exciton state $|A^*B^*\rangle \equiv |11\rangle$. At the present level of approximation, the energy of this state is

$$E^{(2)} = E_1 + E_2. \quad (5)$$

The normalized Einstein coefficients for electric dipole transitions from the heterodimer ground state to the one-exciton levels are

$$\begin{aligned} B_+^{(1)} &= |\langle 00|\mu|+\rangle|^2 = |\langle 00|\mu[c_1|10\rangle + c_2|01\rangle]|^2 \\ &= 1 + 2c_1c_2\hat{\mu}_1 \cdot \hat{\mu}_2 \\ B_-^{(1)} &= |\langle 00|\mu|-\rangle|^2 = |\langle 00|\mu[d_1|10\rangle + d_2|01\rangle]|^2 \\ &= 1 + 2d_1d_2\hat{\mu}_1 \cdot \hat{\mu}_2. \end{aligned} \quad (6)$$

where μ is the total electric dipole moment operator for the heterodimer. Here μ_1, μ_2 are unit vectors that point in the transition moment directions for the lowest allowed electronic transitions on pigments A and B, respectively. It is implicitly assumed in Eq. 6 that the pigments have identical peak absorption coefficients (normalized to unity) for the transition between the ground state and the lowest excited singlet state. The expansion coefficients in Eqs. 1 and 6 are obtained from the matrix of eigenvectors of the Hamiltonian in Eq. 2 (Margenau and Murphy, 1956). Substitution of these into Eqs. 6 leads to explicit expressions for the normalized Einstein coefficients for absorption,

$$\begin{aligned} B_+^{(1)} &= 1 + s\hat{\mu}_1 \cdot \hat{\mu}_2 \\ B_-^{(1)} &= 1 - s\hat{\mu}_1 \cdot \hat{\mu}_2, \end{aligned} \quad (7)$$

where ζ is given by

$$s = \sqrt{\frac{4V^2}{(E_1 - E_2)^2 + 4V^2}}. \quad (8)$$

Equations 7 and 8 show that the resonance interaction redistributes the absorption coefficients between the exciton levels, in a way that depends on the magnitude of V and on the angle between the localized transition moments μ_1 and μ_2. The sum of the normalized absorption coefficients is conserved, $B_+^{(1)} + B_-^{(1)} = 2$. In the limit where $V \to 0$, one recovers the original absorption coefficients of the isolated pigments, $B_+^{(1)} + B_-^{(1)} = 1$.

We now consider the excited-state absorption (ESA) transitions from the one-exciton states $|+\rangle$, $|-\rangle$ to the two-exciton state $|11\rangle$. By analogy to Eq. 6, the normalized absorption coefficients for the ESA transitions $|+\rangle \to |11\rangle$ and $|-\rangle \to |11\rangle$ are, respectively,

$$\begin{aligned} B_+^{(2)} &= |[\langle 10|c_1 + \langle 01|c_2]\mu|11\rangle|^2 = 1 + 2c_1c_2\hat{\mu}_1 \cdot \hat{\mu}_2 \\ B_-^{(2)} &= |[\langle 10|d_1 + \langle 01|d_2]\mu|11\rangle|^2 = 1 + 2d_1d_2\hat{\mu}_1 \cdot \hat{\mu}_2, \end{aligned} \quad (9)$$

which implies (cf. Eq. 6)

$$B_+^{(1)} = B_+^{(2)} \quad B_-^{(1)} = B_-^{(2)}. \quad (10)$$

The transitions among the one- and two-exciton heterodimer levels are shown schematically in Fig. 1.

We next examine the contributions to the absorption difference spectrum upon selective excitation of the one-exciton state $|+\rangle$. The entire one-exciton absorption spectrum (arising from both the $|00\rangle \to |+\rangle$ and $|00\rangle \to |-\rangle$ transitions) will be *uniformly* bleached, because both tran-

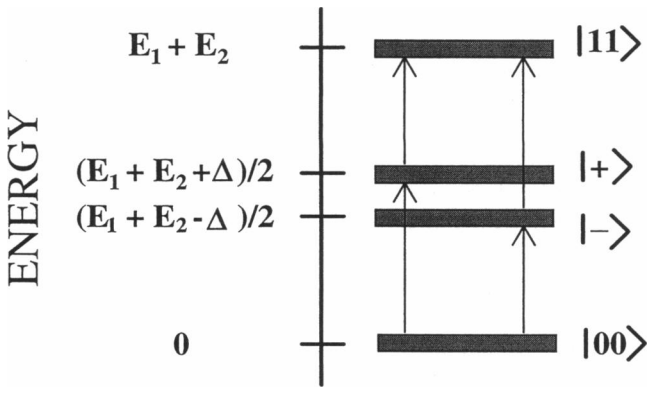

FIGURE 1 Energy levels for a strongly coupled heterodimer. $B_+^{(1)}$, $B_-^{(1)}$ are the Einstein coefficients for absorptive transitions from the ground state to the one-exciton levels. $B_+^{(2)}$, $B_-^{(2)}$ are the Einstein coefficients for excited-state absorption from the one- to two-exciton level.

sitions arise from the common ground state $|00\rangle$. According to Eq. 7, photobleaching (PB) bands will appear with relative absorption changes $(-1 - \varsigma\hat{\mu}_1 \cdot \hat{\mu}_2)$ and $(-1 + \varsigma\hat{\mu}_1 \cdot \hat{\mu}_2)$ at the energies $(E_1 + E_2 + \Delta)/2$ and $(E_1 + E_2 - \Delta)/2$, respectively. This photobleaching spectrum will be *independent* of the excitation wavelength, irrespective of whether $|+\rangle$ or $|-\rangle$ is preferentially excited. However, prompt ESA will occur becase of the transition from the laser-populated one-exciton state level (in this case $|+\rangle$) to the two-exciton state $|11\rangle$. This ESA transition will produce the relative absorption change $(-1 + \varsigma\hat{\mu}_1 \cdot \hat{\mu}_2)$ at the energy $(E_1 + E_2 - \Delta)/2$, according to Eq. 10 and Fig. 1. The resultant sum of PB and ESA spectra will then exhibit a net PB maximum at energy $(E_1 + E_2 + \Delta)/2$ (with relative absorption change $(-1 - \varsigma\hat{\mu}_1 \cdot \hat{\mu}_2)$). It will also exhibit either a net PB or ESA maximum at energy $(E_1 + E_2 - \Delta)/2$ (with relative absorption change $(2\varsigma\hat{\mu}_1 \cdot \hat{\mu}_2)$), depending on the sign of $\hat{\mu}_1 \cdot \hat{\mu}_2$. These contributions to the absorption difference spectrum are shown in perspective in Fig. 2.

In addition, prompt stimulated emission (SE) will be observed from level $|+\rangle$ in a pump-probe experiment. Because the Einstein coefficients for absorption and stimulated emission in a two-level system are equal, the relative peak height of this stimulated emission band will be $(-1 - \varsigma\hat{\mu}_1 \cdot \hat{\mu}_2)$, barring the presence of vibronically induced bands in the ground $\rightarrow$ one-exciton absorption spectrum.

When relaxation occurs between exciton components $|+\rangle$ and $|-\rangle$, the $|+\rangle \rightarrow |11\rangle$ ESA and $|+\rangle \rightarrow |00\rangle$ SE transitions are superseded by $|-\rangle \rightarrow |11\rangle$ and $|-\rangle \rightarrow |00\rangle$ transitions, respectively, with predictable effects on the total absorption difference spectrum (Fig. 3). However, the ground $\rightarrow$ one-exciton absorption spectrum remains uniformly bleached, because relaxation between one-exciton components does not repopulate the heterodimer ground state $|00\rangle$.

We finally consider the weak coupling limit $V \ll |E_1 - E_2|$ in Fig. 4. In this case the parameter $\zeta \rightarrow 0$ (Eq. 8), with the consequence that all of the normalized absorption coefficients $B_+^{(1)}$, $B_-^{(1)}$, $B_+^{(2)}$, $B_-^{(2)}$ are unity. The exciton components $|+\rangle$, $|-\rangle$ now coalesce with the localized states $|10\rangle$, $|01\rangle$ corresponding to excitations on pigments A and B, respectively. Selective excitation of $|+\rangle \equiv |10\rangle$ still bleaches the entire ground $\rightarrow$ one-exciton absorption spectrum, yielding PB components of equal intensity at the energies $E_+^{(1)} = E_1$ and $E_-^{(1)} = E_2$. However, the prompt $|+\rangle \rightarrow |11\rangle$ ESA transition, which occurs at the excitation energy E_2 for pigment B (cf. Fig. 1), exactly cancels the PB component at that energy. Hence the net absorption difference spectrum (aside from SE) empirically shows selective photobleaching of pigment A, in accordance with our intuitive expectations for an uncoupled heterodimer.

Although it is useful for illustrating the transition between the strong and weak coupling cases, the heterodimer problem is uncharacteristically simple because it has only one two-exciton state. In a system containing N strongly coupled pigments, there will be $N(N - 1)/2$ two-exciton basis functions, i.e., $|A^*B^*C^*\ldots\rangle$, $|A^*\ B C^*\ldots\rangle$, $|AB^*C^*\ldots\rangle$, etc. (Lin et al., 1991). An $N \times N$ matrix must

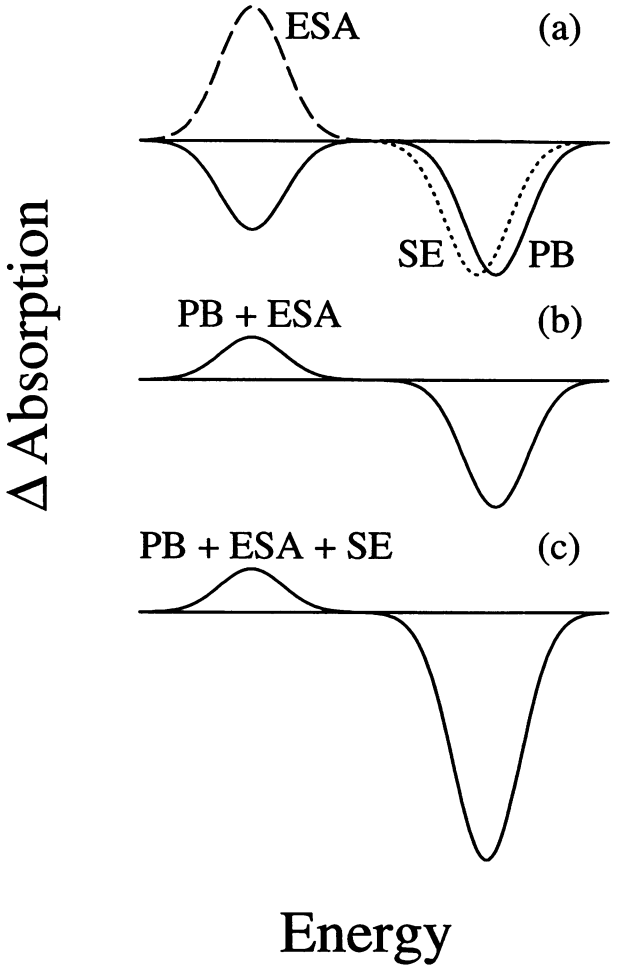

FIGURE 2 Schematic absorption difference signals for a strongly coupled heterodimer with $\zeta\hat{\mu}_1 \cdot \hat{\mu}_2 = 0.4$, excited to its one-exciton component $|+\rangle$. (*a*) Photobleaching, excited-state absorption, and stimulated emission signals, denoted by solid, dashed, and dotted curves, respectively. (*b*) Sum of photobleaching and excited-state absorption signals. (*c*) Total absorption difference spectrum.

be diagonalized to obtain the one-exciton levels, and an $[N(N - 1)/2] \times [N(N - 1)/2]$ matrix must be diagonalized to find the two-exciton levels. For example, determining the two-exciton levels for the 21 BChl *a* pigments in an FMO trimer requires diagonalization of a 210×210 matrix. The net absorption difference spectrum (apart from SE) will then contain ESA transitions at new energies that do not appear in the PB spectrum. Fortunately, evaluating the $[N(N - 1)/2] \times [N(N - 1)]/2$ Hamiltonian matrix in the two-exciton basis requires no new information beyond that contained in the $N \times N$ one-exciton Hamiltonian.

THE *N*-PIGMENT SYSTEM

The total electronic Hamiltonian for N coupled pigments is

$$\hat{H} = \sum_{p}^{N} \hat{H}_p + \sum_{p<q}^{N} V_{pq}, \qquad (11)$$

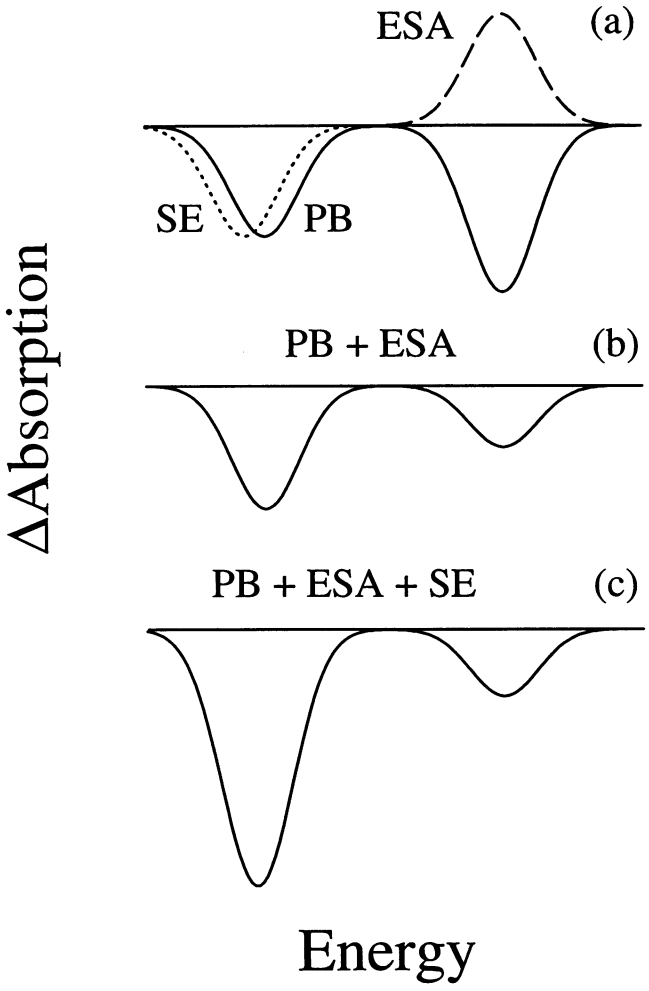

FIGURE 3 Absorption difference signals for a strongly coupled heterodimer with $\zeta\hat{\mu}_1 \cdot \hat{\mu}_2 = 0.4$, excited to its one-exciton component $|-\rangle$. Legend is the same as in Fig. 2.

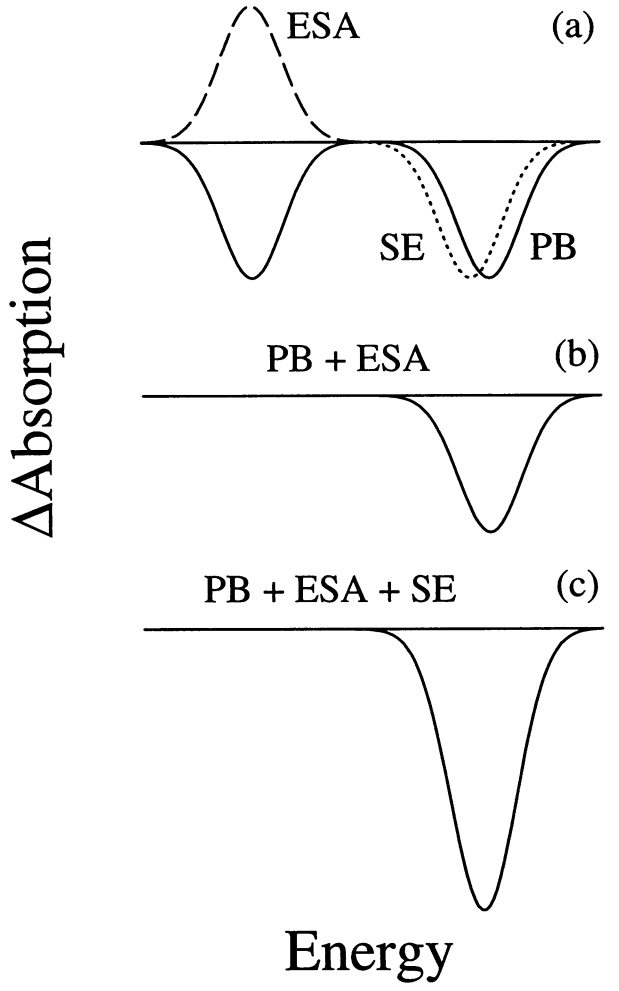

FIGURE 4 Absorption difference signals for a weakly coupled heterodimer ($\zeta \approx 0$) under excitation of the localized state $|+\rangle \equiv |10\rangle$. Legend is the same as in Fig. 2.

where $\hat{H}_p$ is the electronic Hamiltonian for pigment p and V_{pq} represents the interaction between pigments p and q. The N one-exciton states can be expanded in terms of the localized states $|A^*BC\ldots\rangle$, $|AB^*C\ldots\rangle$, $|ABC^*\ldots\rangle$, etc. For simplicity, we will use $|\chi_i^{(1)}\rangle$ to denote the one-exciton basis function that localizes the excitation on pigment i, i.e., $|\chi_1^{(1)}\rangle = |A^*BC\ldots\rangle$, $|\chi_2^{(1)}\rangle = |AB^*C\ldots\rangle$, etc. The one-exciton states $|\psi_i^{(1)}\rangle$ and their energies $E_i^{(1)}$ are obtained by diagonalizing the $N \times N$ Hamiltonian matrix with elements

$$H_{ij} = \left\langle \chi_i^{(1)} \middle| \sum_{p=1}^{N} \hat{H}_p + \sum_{p<q}^{N} V_{pq} \middle| \chi_j^{(1)} \right\rangle. \tag{12}$$

The diagonal elements of this matrix are $H_{ii} = E_i$, the lowest excited state energies of pigments i in the absence of resonance interactions. The off-diagonal elements ($i \neq j$) are

$$H_{ij} = \langle \chi_i^{(1)} | V_{ij} | \chi_j^{(1)} \rangle \equiv V_{ij}, \tag{13}$$

because all other contributions in Eq. 12 vanish through orthogonality. For pigments i, j with separation large compared to the molecular size, and with excited states connected to the ground states by strongly allowed electric dipole transitions, $\langle V_{ij} \rangle$ is dominated by the dipole-dipole interaction. For pigments that are ~10 Å apart (as in the case of the nearest neighbors in FMO trimers), contributions from higher-multipole interactions gain importance. The expansion coefficients c_j^i in the one-exciton states

$$|\psi_i^{(1)}\rangle = \sum_{j=1}^{N} c_j^i |\chi_j^{(1)}\rangle \tag{14}$$

(which are appear in the Hamiltonian matrix of eigenvectors) may be used to calculate the absorption coefficients $B_i^{(1)}$ for the absorption lines corresponding to transitions from the N-pigment ground state $|000\ldots0\rangle$ to the one-exciton states $\psi_i^{(1)}$,

$$\begin{aligned} B_i^{(1)} &= \left| \sum_j c_j^i \langle 000\ldots0 | \mu | \chi_j^{(1)} \rangle \right|^2 \\ &= |c_1^i \hat{\mu}_1 + c_2^i \hat{\mu}_2 + \cdots + c_N^i \hat{\mu}_N|^2. \end{aligned} \tag{15}$$

Here the unit vectors $\hat{\mu}_j \equiv \langle 0|\mu_j|\chi_j^{(1)}\rangle$ give the transition moment directions for the lowest electronic transitions on pigments j.

The $N(N-1)/2$ two-exciton states $\psi_i^{(2)}$ are expanded in the set of the $N(N-1)/2$ basis functions $|\chi_{12}^{(2)}\rangle = |A^*B^*C\cdot\ldots\rangle$, $|\chi_{13}^{(2)}\rangle = |A^*BC^*\ldots\rangle$, $|\chi_{23}^{(2)}\rangle = |AB^*C^*\ldots\rangle$, etc. Their energies $E_i^{(2)}$ are obtained by diagonalizing the matrix of the Hamiltonian (Eq. 11) in this doubly excited basis. The relevant matrix elements are easily seen to be

$$\begin{aligned}\langle\chi_{ij}^{(2)}|\hat{H}|\chi_{ij}^{(2)}\rangle &= E_i + E_j\\ \langle\chi_{ij}^{(2)}|\hat{H}|\chi_{ik}^{(2)}\rangle &= V_{jk}, \quad j \neq k\\ \langle\chi_{ij}^{(2)}|\hat{H}|\chi_{kl}^{(2)}\rangle &= 0, \quad i \neq k, l; \quad j \neq k, l.\end{aligned} \tag{16}$$

In this basis, the diagonal matrix elements are pairwise sums of single-pigment excitation energies E_i, E_j. The nonzero off-diagonal matrix elements V_{jk} in Eq. 16 are identical to off-diagonal matrix elements that arise in the one-exciton basis (Eq. 13). For illustration, Table 1 gives the 21×21 two-exciton Hamiltonian matrix for an arbitrary system of seven pigments (e.g., the seven BChl *a* pigments enclosed by one subunit of the FMO protein). For this Hermitian (real symmetric) matrix, only the elements on and above the diagonal are shown. This general two-exciton matrix becomes further simplified in specialized cases (e.g., one-dimensional J-aggregates in which only nearest-neighbor resonant interactions are considered). The two-exciton states in this approximation are linear combinations of the doubly excited basis functions $|\chi_{ij}^{(2)}\rangle$, i.e.,

$$|\psi_k^{(2)}\rangle = \sum_{ij} d_{ij}^k |\chi_{ij}^{(2)}\rangle, \tag{17}$$

where the real-valued coefficients d_{ij}^k are taken from the matrix of eigenvectors of the real symmetric two-exciton Hamiltonian. The absorption coefficient for any given one- to two-exciton ESA transition $|[\psi_i^{(1)}\rangle \rightarrow |\psi_k^{(2)}\rangle$ is then straightforwardly computed via

$$B_{l\rightarrow k}^{(2)} = |\langle\psi_l^{(1)}|\mu|\psi_k^{(2)}\rangle|^2 = \left|\sum_{ijm} d_{ij}^k c_m^l \langle\chi_m^{(1)}|\mu|\chi_{ij}^{(2)}\rangle\right|^2, \tag{18}$$

where it is clear from the definition of the singly and doubly excited basis functions that

$$\langle\chi_m^{(1)}|\mu|\chi_{ij}^{(2)}\rangle = \hat{\mu}_j\delta_{im} + \hat{\mu}_i\delta_{jm}. \tag{19}$$

At least one of the terms always vanishes on the left-hand side of Eq. 19, because the doubly excited basis functions $|\chi_{ij}^{(2)}\rangle$ are undefined for $i = j$.

The normalized absorption coefficients for transitions from the ground state to the one-exciton states $\psi_i^{(1)}$ obey the sum rule

$$\sum_{i=1}^{N} B_i^{(1)} = N. \tag{20}$$

The absorption coefficients for the one-exciton $\rightarrow$ two-exciton transitions $\psi_i^{(1)} \rightarrow \psi_j^{(2)}$ similarly obey the sum rule:

$$\sum_{i=1}^{N}\sum_{j=1}^{N} B_{i\rightarrow j}^{(2)} = N(N-1). \tag{21}$$

This implies that the mean sum of absorption coefficients for all one-exciton $\rightarrow$ two-exciton transitions originating

TABLE 1 Two-exciton Hamiltonian for an arbitrary seven-pigment system*

12	23	24	25	26	27	13	14	15	16	17	0	0	0	0	0	0	0	0	0	0
	13	34	35	36	37	12	0	0	0	0	14	15	16	17	0	0	0	0	0	0
		14	45	46	47	0	12	0	0	0	13	0	0	0	15	16	17	0	0	0
			15	56	57	0	0	12	0	0	0	13	0	0	14	0	0	16	17	0
				16	67	0	0	0	12	0	0	0	13	0	0	14	0	15	0	17
					17	0	0	0	0	12	0	0	0	13	0	0	14	0	15	16
						23	34	35	36	37	24	25	26	27	0	0	0	0	0	0
							24	45	46	47	23	0	0	0	25	26	27	0	0	0
								25	56	57	0	23	0	0	24	0	0	26	27	0
									26	67	0	0	23	0	0	24	0	25	0	27
										27	0	0	0	23	0	0	24	0	25	26
											34	45	46	47	35	36	37	0	0	0
												35	56	57	34	0	0	36	37	0
													36	67	0	34	0	35	0	37
														37	0	0	34	0	35	36
															45	56	57	46	47	0
																46	67	45	0	47
																	47	0	45	46
																		56	67	57
																			57	56
																				67

*Generated using Eqs. 16, with 21 doubly excited basis functions $\chi_{ij}^{(2)}$ ordered as follows: χ_{12}, χ_{13}, χ_{14}, χ_{15}, χ_{16}, χ_{17}, χ_{23}, χ_{24}, χ_{25}, χ_{26}, χ_{27}, χ_{34}, χ_{35}, χ_{36}, χ_{37}, χ_{45}, χ_{46}, χ_{47}, χ_{56}, χ_{57}, χ_{67}. Boldface entries **ij** represent diagonal elements $E_i + E_j$; other entries *ij* represent off-diagonal elements V_{ij} (see text).

from a particular one-exciton state $\psi_i^{(1)}$, averaged over the N one-exciton states, has the intuitively reasonable value

$$\left\langle \sum_{j=1}^{N} B_{i\to j}^{(2)} \right\rangle = N - 1. \tag{22}$$

FMO TRIMERS

The bacteriochlorophyll *a* protein trimer from the green sulfur bacterium *Prosthecochloris aestuarii* has been widely studied as a prototypical, strongly coupled antenna (Pearlstein and Hemenger, 1978; Philipson and Sauer, 1972; Olson et al., 1976; Johnson and Small, 1991; Pearlstein, 1992; Lu and Pearlstein, 1993; Savikhin and Struve, 1994). The basic structural unit contains three identical protein subunits, in the form of folded β-sheets enclosing seven BChl *a* pigments each (Matthews and Fenna, 1980). If the pigment organization and the ground and Q_y electronic wavefunctions are known, the off-diagonal matrix elements V_{ij} can be evaluated for all 210 pigment pairs in the trimer. In our simulations, we use the interactions V_{ij} computed by Pearlstein (1992). These were evaluated using the point monopole method, with BChl *a* Q_y transition charge distributions taken from Weiss (1972). The pigment positions and orientations are from the crystal structure of Tronrud et al. (1986). The BChl *a* diagonal energies E_i are not directly observable. Pearlstein and co-workers varied the seven independent diagonal energies to yield best fits to empirical absorption and circular dichroism (CD) spectra. However, minor variations in the experimental spectra can translate into significant changes in the optimal diagonal energies and wavefunctions. For example, best fits to the optical spectra of Philipson and Sauer (1972; hereafter PS) suggest that BChl 3 has the lowest diagonal energy, in the pigment numbering scheme of Matthews and Fenna (1980). Best fits to the spectra of Olson et al. (1976; hereafter OKT) suggest that the lowest-energy pigment is BChl 7 instead (Lu and Pearlstein, 1993). Very recently, D. Gülen (unpublished work) has suggested that optimal fits to absorption, LD, and singlet-triplet absorption difference (STAD) spectra would provide a more incisive criterion for FMO simulations than absorption and CD spectra. Simultaneous fits to the absorption, LD, and STAD spectra are obtained when the lowest diagonal energy is assigned to BChl 6. These examples serve to illustrate that the FMO electronic structure remains unsettled; Gülen's study and recent spectroscopic work (van Mourik et al., 1994) may stimulate renewed interest in this problem. In our calculations, we will use both the PS and OKT diagonal energies (Lu and Pearlstein, 1993). Fig. 5 shows the wavelength positions of the one-exciton levels obtained by diagonalizing the PS and OKT Hamiltonian matrices. These levels are compared with the respective sets of input diagonal energies. Our exciton level numbering scheme is that of Pearlstein (1992) and Lu and Pearlstein (1993), where the highest and lowest energy levels are denoted 1 and 21, respectively. Because the interactions between BChl pigments belonging to different subunits are small compared to the largest interactions between pigments belonging to the same subunit, the exciton levels tend to be clustered in groups of three. Under the C_3 symmetry of the FMO trimer, each group is split into a nondegenerate level and a doubly degenerate pair of levels. In Fig. 5 we use *A* to denote the lowest three levels (19–21), *B* to denote the next three levels (16–18), etc. The OKT diagonal energies for pigments 2–5 are closely spaced between 798 and 803 nm, whereas those for pigments 1, 6, and 7 are well separated. The lowest OKT diagonal energy belongs to pigment 7. In the PS simulation, pigment 3 exhibits the lowest diagonal

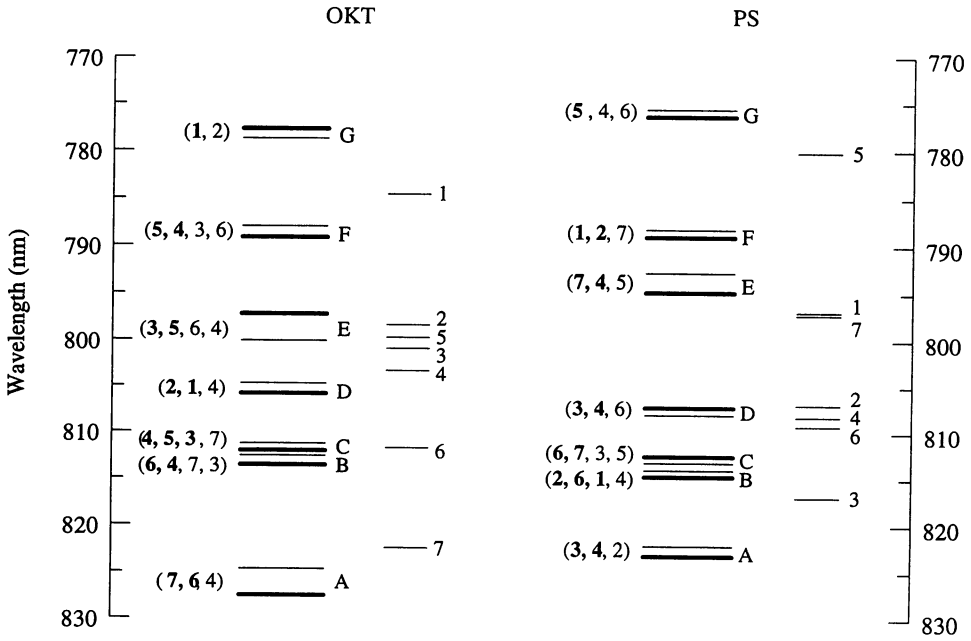

FIGURE 5 Exciton levels and diagonal energies (*long* and *short bars*, respectively) for the OKT and PS Hamiltonians for FMO trimers from *P. aestuarii*. Successive groups of three exciton levels are labeled *A*, *B*, . . . , *G* in order of energy; thicker bars represent doubly degenerate levels. Numbers in parentheses indicate BChl pigments collectively exhibiting >75% of the excitation density in each group; boldface numbers show pigments containing >50% of the density. Diagonal energies are labeled with corresponding BChl pigment numbers.

energy. Fig. 5 also shows the BChl pigments whose excitations make the largest contributions to each group of exciton levels. In particular, the BChl pigments that are collectively responsible for >75% of the total occupation numbers in each group (*A*, *B*, etc.) are shown in parentheses.

In addition to the one- and two-exciton Hamiltonians (which are 21 × 21 and 210 × 210 matrices, respectively, in the FMO trimer), single-pigment absorption and stimulated emission profiles are needed for the BChl *a* ground → Q_y transition. These have been determined for BChl *a* monomers in polar solvents (Becker et al., 1991), but they are unknown for the pigments in FMO trimers. Lu and Pearlstein simulated the absorption and CD spectra of Olson et al. (1976) by assigning spectral widths of 95–342 cm^{-1} to symmetric Gaussian FMO exciton components. Fits of their theoretical spectra to the low-temperature spectra of Philipson and Sauer (1972) yielded component widths ranging from 185 to 354 cm^{-1}. In either case, the spectral widths are far narrower than the inhomogeneous broadening (~500 cm^{-1}) observed for BChl *a* in alcohols (Becker et al., 1991). In the present simulations, we have arbitrarily used a symmetrical Gaussian profile with 150 cm^{-1} bandwidth to represent each spectral component in the ground → one-exciton PB transitions and in the one-exciton → two-exciton ESA transitions. ESA arising from BChl *a* transitions from the Q_y state to higher S_n states was not included. The spectrum of this monomeric ESA is several times broader than the inhomogeneous widths of the steady-state absorption and fluorescence spectra in polar solvents (Becker et al., 1991). Hence, including monomeric ESA would result primarily in a positive baseline shift in the entire ΔA spectrum, without materially altering its structure. Whereas a large Stokes shift is observed between the BChl *a* Q_y absorption and stimulated emission band maxima for BChl *a* in alcohols, a similar shift is not expected for BChl *a* pigments in the hydrophobic interior of the FMO protein. The stimulated emission profile for each one-exciton level is therefore represented by a symmetrical Gaussian profile congruent with the corresponding absorption profile, because the integrated Einstein coefficients for absorption and stimulated emission are equal in the absence of distortions in equilibrium geometry.

Typical OKT simulations of absorption difference spectra are shown in Fig. 6 for FMO trimers from *P. aestuarii*. These are prompt absorption difference spectra, obtained using the excitation wavelengths (from top) 780, 790, 815, and 825 nm. The left- and right-hand columns were obtained using zero and nonzero off-diagonal matrix elements V_{ij}, respectively. The left-hand column thus shows the absorption difference spectra predicted in the absence of resonance couplings. The latter spectra are *not* the ones that would be observed if exciton coherence decays rapidly during the time scale of observation (see below); they simply represent a fictitious FMO complex with noninteracting pigments. In this idealized case, the evolution in the prompt absorption difference spectrum that accompanies laser tuning across the FMO Q_y spectrum resembles red-

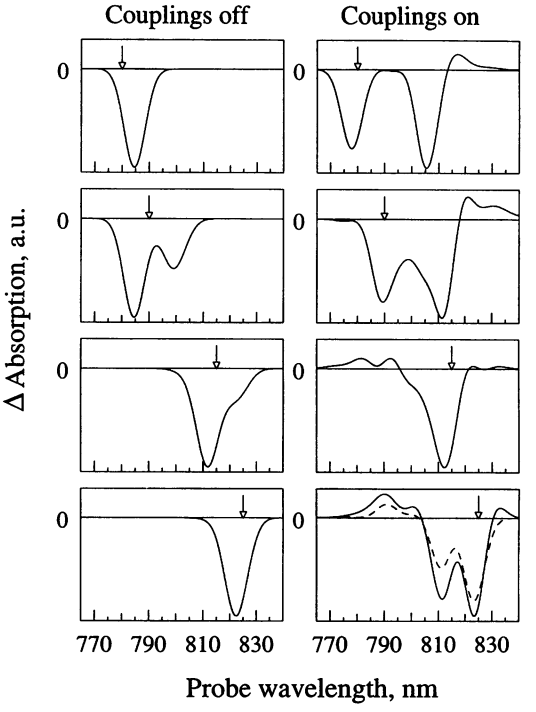

FIGURE 6 OKT prompt absorption difference spectra for FMO trimers from *P. aestuarii*, for the excitation wavelengths 780, 790, 815, and 825 nm (indicated by *arrows*). Left-hand column shows spectra obtained using zero off-diagonal Hamiltonian matrix elements; right-hand column shows spectra obtained using using off-diagonal Hamiltonian matrix elements from Pearlstein (1992). ΔA units are arbitrarily but mutually normalized. Positive and negative signals correspond to ESA and PB/SE, respectively. Dashed curve in lower right panel shows absorption difference spectrum for trimer with excitation localized on BChl 7 (one of three equivalent pigments has the lowest diagonal energy in the OKT description).

shifting of a monomeric BChl *a* absorption difference spectrum. (The dual peak under 790-nm excitation arises only because this wavelength lies between diagonal energies at 784 nm (pigment 1) and 798–803 nm (pigments 2–5); cf. Fig. 5.) When the resonance interactions are turned on (right-hand column in Fig. 6), the spectral evolution becomes more complicated. Secondary PB/SE "maxima" now appear at wavelengths considerably removed from the excitation wavelength. These maxima physically stem from gaps in the one-exciton → two-exciton ESA spectrum, which otherwise tends to cancel much of the photobleaching of the Q_y steady-state absorption spectrum. Of particular interest is the spectrum excited at 825 nm. This wavelength produces near-selective excitation of the lowest three exciton levels (group *A*), because the next higher group of OKT levels is centered near 812–813 nm. Unlike the ΔA spectrum excited at 825 nm in the absence of resonance interactions, this spectrum shows a prominent secondary PB/SE peak at ~812 nm.

We next show sets of OKT and PS absorption difference spectra (Figs. 7 and 8, respectively), averaged over each of the exciton level groups *A* through *G* (only minor variations are observed between the nondegenerate and doubly degen-

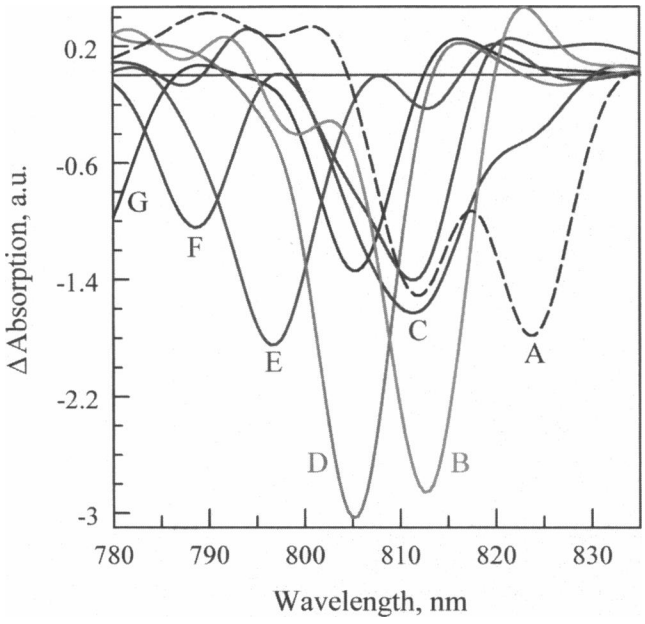

FIGURE 7 OKT Q_y absorption difference spectra for FMO trimers. Each ΔA spectrum is averaged over one of the groups of levels *A–G* (cf. Fig. 5).

erate ΔA spectra within each level group; not shown). The physical differences between the OKT and PS ΔA spectra are considerable, even though the OKT and PS Hamiltonians yield somewhat similar absorption and CD spectra (Lu and Pearlstein, 1993). The OKT ΔA spectrum averaged over exciton levels 19–21 (group *A*) shows dual PB/SE peaks at ~825 and ~812 nm. (In this regard, this spectrum resembles the prompt OKT spectrum excited at 825 nm in Fig. 6.)

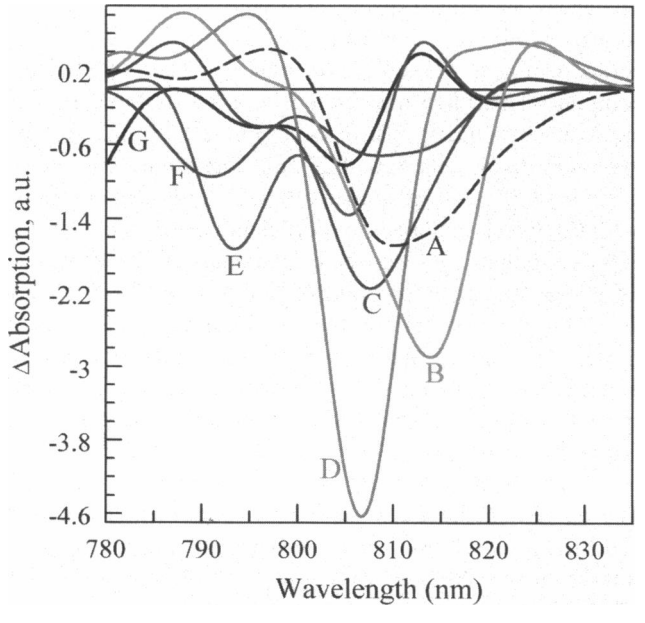

FIGURE 8 PS Q_y absorption difference spectra. Each ΔA spectrum is averaged over one of the groups of levels *A–G* (cf. Fig. 5).

The corresponding PS ΔA spectrum for group *A* shows only a single broad PB/SE peak at ~810 nm. There are close similarities between these spectra (which were computed for the 21 pigments in the FMO trimer) and the corresponding spectra for seven pigments enclosed within one subunit of the trimer (not shown) in the case of both the PS and the OKT simulations. The differences are limited primarily to minor variations in relative peak intensities. This point is relevant because FMO trimers from *Cb. tepidum* exhibit pump-probe anisotropy decay components with lifetimes (1.7–2.0 ps at room temperature) that have no counterpart in the isotropic kinetics (Savikhin et al., 1994; Savikhin and Struve, 1994). These components may thus arise from energy transfers between equivalent states belonging to different subunits, i.e., the original exciton states may evolve early into states that are localized within one group of seven pigments.

Experimental absorption difference spectra were obtained for FMO trimers isolated from *Cb. tepidum* according to Olson (1976), with the modifications described by Savikhin et al. (1994). The room temperature absorption spectrum (with peaks at 809, 602, 371, and 262 nm) is very similar to those of FMO trimers isolated from other green photosynthetic bacteria (Blankenship et al., 1993). These experiments were performed at 19 K, to resolve spectral features arising from well-defined groups of exciton transitions (Philipson and Sauer, 1972; Olson et al., 1976). The self-mode-locked Ti:sapphire laser and pump-probe optics have been described elsewhere (Savikhin and Struve, 1994; Savikhin et al., 1994). The radio frequency (RF) multiple modulation detector and electronics were replaced by a new design, in which the probe beam-detecting photodiode was incorporated into an RLC input loop tuned to the RF detection frequency (Savikhin, 1995). Samples were housed between two optical flats spaced by 0.5 mm, in a window assembly in thermal contact with the end of a 2.25-cm-diameter Cu cold finger in an Air Products (Allentown, PA) DE202 closed-cycle He expander module. The sample temperature was monitored directly using a calibrated Cu-constantan (type T) thermocouple placed at the center of the cell. Because quartz exhibits poor thermal conductivity, and because sapphire exhibits birefringence that can interfere with anisotropy studies, one window of each material was used. The laser beams traversed the quartz window before entering the sample and then exited through the sapphire window. The latter contacted the Cu window mount through an foil gasket. In this way, the temperature differential between the sample and the cold finger was only 6 K when the latter was 13 K; the temperature differential was reduced to 1 K at 100 K. In most experiments, the excitation pulses (generated by passing the Ti:sapphire output spectrum through a CVI Corp. IF790 bandpass interference filter; Savikhin and Struve, 1994) were centered at 789 nm with 6-nm bandwidth. The probe pulse spectra (which are superimposed on the low-temperature FMO absorption spectrum in Fig. 9) were centered at ~5-nm intervals from ~780 to ~835 nm. These spectra were shaped using an IF820 inter-

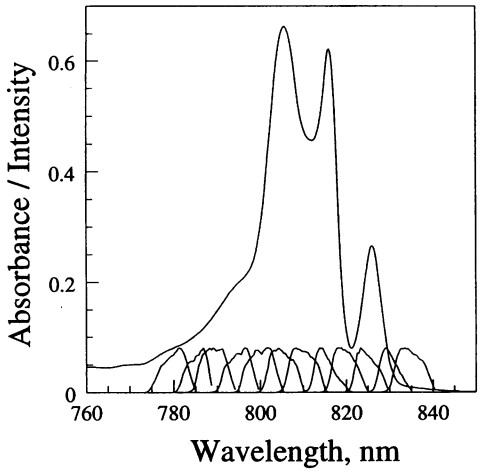

FIGURE 9 Steady-state absorption spectrum of FMO trimers from *Cb. tepidum* at 19 K. Laser spectra are superimposed for 789-nm pump pulses, and for probe pulses centered at 5-nm intervals from 780 to 835 nm.

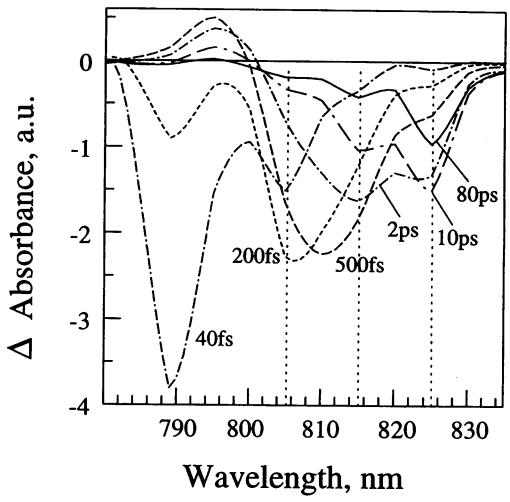

FIGURE 10 Slices at fixed time delays (40 fs to 80 ps) of cubic spline fit to a three-dimensional absorption difference versus time and wavelength surface, assembled from 12 two-color profiles under 789-nm excitation of FMO trimers from *Cb. tepidum* at 19 K. Positive and negative signals correspond to ESA and PB/SE, respectively.

ference filter (for wavelengths 780 through 815 nm) and an IF850 filter (for wavelengths 815 through 835 nm). Probe wavelength tuning was accomplished by tilting the filters. The pump and probe pulse spectra (Fig. 9) were measured during experiments using a Czerny-Turner monochromator (7.9 nm/mm dispersion), with its output imaged onto the linear CCD array of a Unidata BP2048 beam profiler. The precision in the relative amplitudes of pump-probe profiles for different pump-probe wavelength combinations was not worse than 5–10%. The laser cross-correlation (measured in situ using a zero-background $LiIO_3$ crystal) was typically 200–250 fs FWHM.

Twelve two-color profiles were accumulated in both 8- and 80-ps windows under 789-nm excitation at 19 K, using the probe wavelengths from 780 to 835 nm. These profiles were assembled to generate a three-dimensional grid of absorption difference versus time and wavelength. Cross sections of a cubic spline fit to this grid are shown for several time delays from 40 fs to 80 ps in Fig. 10. At 40 fs, most of the nominal photobleaching/stimulated emission (PB/SE) appears near the 789-nm excitation wavelength; however, the spectrum at this time already exhibits a well-resolved PB/SE peak at ~805 nm. Considerable spectral evolution subsequently occurs, culminating in an equilibrated spectrum (≥10 ps) with much of the PB/SE concentrated near 825 nm. The evolving spectra exhibit considerable structure throughout, with major PB/SE features near 805 and 815 as well as 790 and 825 nm. They are similar to absorption difference spectra that have very recently been measured by Freiberg et al. (1996), except that our higher time resolution allows the identification of more lifetime components in kinetic analyses (see below).

For global analysis, 11 composite two-color profiles were assembled by combining 8- and 80-ps window profiles for the probe wavelengths 785 through 835 nm. In these global fits, relative χ^2 weighting factors of 10 and 1 were used for data points in the intervals (−2 ps, 8 ps) and (8 ps, 78 ps), respectively. This ensured fitting of short-lifetime as well as long-lifetime components. Two additional profiles with 566-ps windows (probe wavelengths 815 and 830 nm) were added to help define the longest-lifetime components. Six lifetimes (170 fs, 630 fs, 2.5 ps, 11 ps, 74 ps, and 840 ps) sufficed to attain quality global fits in all 13 profiles for times greater than 100 fs. Whereas spectral equilibration occurs with femtosecond kinetics at room temperature (Savikhin and Struve, 1994), recent 812 → 829 nm two-color experiments on FMO trimers from *Cb. tepidum* have shown that the slowest equilibration steps are decelerated into the picosecond regime at 19 K (Savikhin and Struve, 1996). The decay-associated spectra (DAS) for the six lifetimes are shown in Fig. 11. For example, a 170-fs PB/SE decay component near 795 nm is mirrored by a 170-fs PB/SE rise component near 815 nm. Similarly, a 630-fs DAS exhibits negative amplitudes (PB/SE decay) near 805 nm, and positive amplitudes near 820–825 nm. The longest component lifetime (840 ps) is, of course, not well defined in our global analysis, which included no profiles in windows longer than 566 ps. Comparisons may be drawn between the absorption difference spectra at long times (10 and 80 ps in Fig. 10) and the simulated spectra for the lowest three exciton levels (group *A* in Figs. 7 and 8), where excitations should accumulate in a Boltzmann distribution at 19 K. The OKT spectrum for the group *A* levels resembles the experimental spectrum at 10 ps; both spectra exhibit PB/SE peaks at ~825 nm and 812–815 nm, with similar relative intensities. The agreement between the 10-ps experimental spectrum and the PS simulation for the group *A* levels, whose long-wavelength PB/SE spectrum is dominated by a broad peak centered at ~810 nm, is considerably poorer.

Between 10 and 80 ps, the shape of the experimental spectrum (Fig. 10) evolves primarily through diminution of

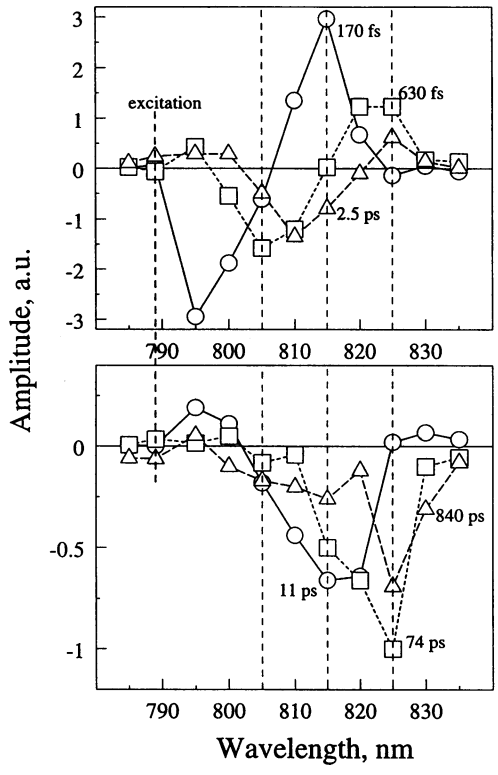

FIGURE 11 Decay-associated spectra (DAS) obtained from global fit to two-color absorpton difference profiles under 789-nm excitation of FMO trimers from *Cb. tepidum*. Horizontal coordinate is probe wavelength. Positive and negative DAS amplitudes correspond to PB/SE decay and rise components, respectively.

the 815-nm PB/SE signal relative to the primary PB/SE peak at 825 nm. This process is connected with the 11-ps DAS spectrum in Fig. 11. In the lower right-hand panel of Fig. 6, we contrast the prompt absorption difference spectrum of the FMO complex excited at 825 nm (which is dominated by excitations in group *A* levels, *solid curve*) with the spectrum to be expected when the Q_y excitation is localized on pigment 7 (*dashed curve*). The latter spectrum was evaluated by replacing the usual one-exciton → two-exciton ESA spectrum with the absorption spectrum of the 20 coupled pigments other than pigment 7 (obtained by diagonalizing an $(N-1)\times(N-1)$ OKT Hamiltonian that excludes pigment 7). In additon, the SE peak is centered at the diagonal energy of pigment 7, rather than at the mean energy of the exciton levels in group *A*. The difference between the "excitonic" and "localized" spectra in Fig. 6 resembles the 11-ps component of spectral evolution in Figs. 9–10, suggesting that exciton localization may be an origin of this lifetime in the global analysis. (The DAS spectrum of this component, unlike those of shorter-lifetime components, which are clearly associated with downhill energy transfers in Fig. 9, exhibits no regions with large positive amplitudes reflecting PB/SE growth, only negative amplitudes in the neighborhood of 815 nm.) However, such conclusions are premature, because 1) the diagonal energies in FMO trimers from *P. aestuarii* are still uncertain—the true assignments could differ materially from those in both the PS and OKT simulations; and 2) there may be significant differences between the electronic structures of FMO trimers from *P. aestuarii* and *Cb. tepidum*. Although the positions of the longest-wavelength absorption bands (near 825, 815, and 805 nm) are similar for both species at low temperature, their relative absorption coefficients differ.

The simulated absorption difference spectra in Fig. 7 or 8 may be combined with a kinetic model for relaxation between groups of exciton levels to generate a three-dimensional surface of ΔA versus time and probe wavelength. In Fig. 12 we compare two such surfaces (generated from the OKT simulation, in the presence and absence of resonance couplings) with the experimental absorption difference surface for FMO trimers excited at 19 K at 789 nm. The pertinent kinetic models are shown in Fig. 13. In the presence of resonance couplings, group *F* levels excited near 790 nm relax within 100 fs to the group *D* levels, which are responsible for the steady-state absorption band near 805 nm. The group *D* levels then branch 50% into the group *B* and *C* levels bunched near 815 nm (with 170-fs kinetics) and 50% into the group *A* levels at 825 nm (with 630-fs kinetics). After the former step, the excitations are equally distributed between groups *B* and *C*. Finally, the group *B* and *C* levels relax into the group *A* levels with 2.5-ps kinetics. The OKT simulation that includes resonance couplings reproduces some of the major features in the experimental ΔA spectrum. The simulation that omits resonance couplings fails to generate realistic ΔA surfaces, primarily because it cannot mimic the bimodal long-time absorption difference spectrum with PB/SE maxima at ~815 amd 825 nm (cf. Fig. 6). Neither simulation predicts the intense experimental "PB/SE" maximum that occurs near zero time and 790 nm (Fig. 12), but this discrepancy is to be expected because FMO trimers exhibit intense coherent coupling artifacts arising from electronic coherence in one-color experiments (Savikhin and Struve, 1994; Chachisvilis and Sundström, 1996). PS simulations (not shown in Fig. 12) yielded far less realistic ΔA surfaces than the OKT simulations did for any kinetic model.

Simulation of the very early relaxation kinetics (<100 fs) is problematic, even when using the OKT model. By 40 fs, a secondary PB/SE peak appears at ~805 nm, in addition to the intense signal that overlaps the pump wavelengths (Fig. 10). The simulated ΔA spectra for the levels excited near 789 nm (group *F*) exhibit no secondary feature near 805 nm (Fig. 7); the group *E* levels do show a large PB/SE peak at this wavelength. These factors prompted us to model the early kinetics with the sequential 30-fs and 70-fs steps shown in Fig. 13. Our need to postulate these steps may be an artifact of applying our OKT simulations to FMO trimers from *Cb. tepdium*, because their electronic structure (particularly in the higher exciton levels) may differ considerably from those in *P. aestuarii* (Reddy et al., 1995). It may well be that the prompt ΔA spectrum of *Cb. tepidum* levels excited at 789 nm exhibits a major "PB/SE" feature near 805 nm, unlike the OKT spectrum for the group *F* levels

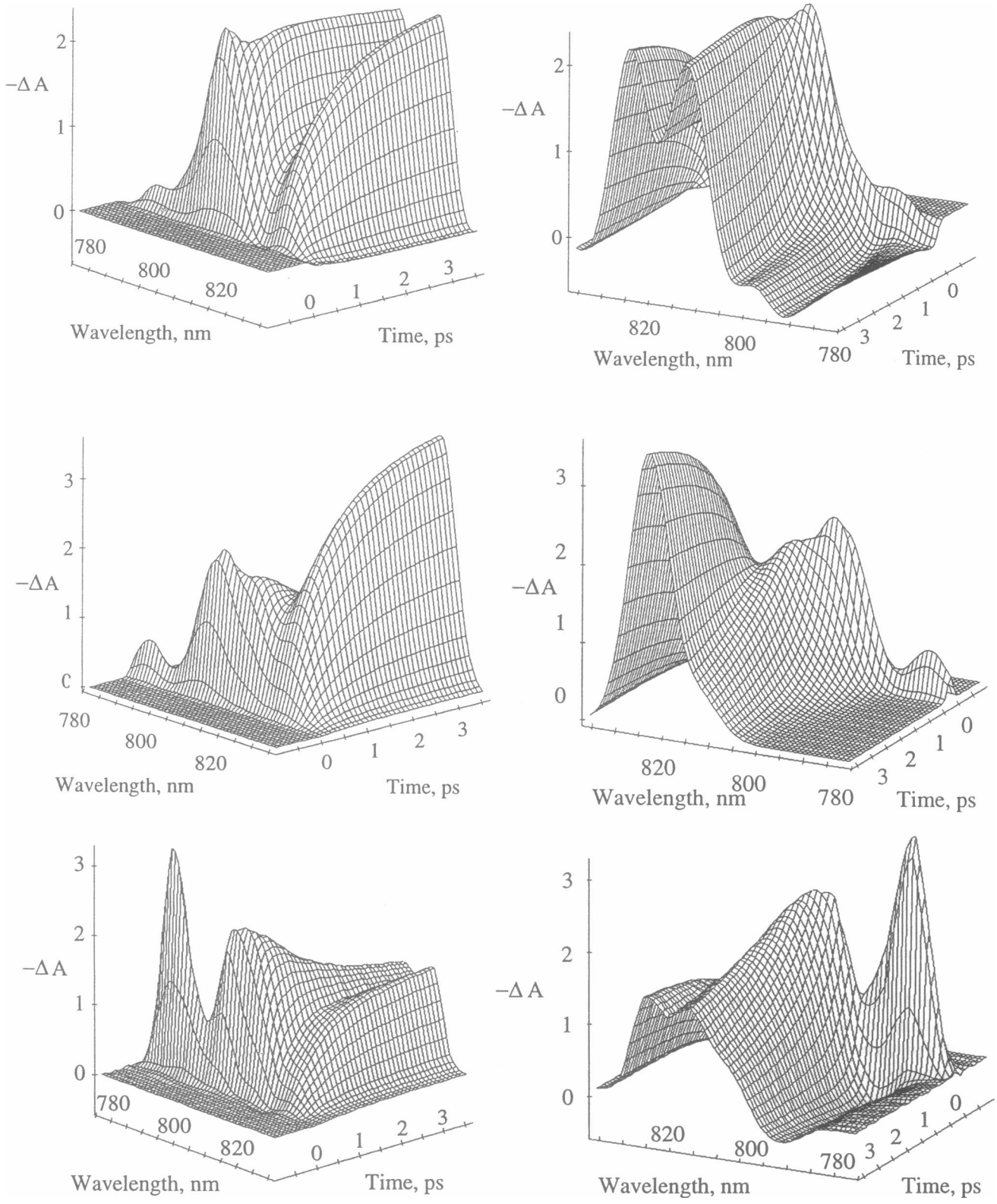

FIGURE 12 Three-dimensional surfaces of absorption difference versus time and probe wavelength for FMO trimers excited at 789 nm: OKT simulation with resonance couplings (*top*), OKT simulation without resonance couplings (*center*), and experimental (*bottom*). For ease of visualization, the positive vertical axis corresponds to PB/SE. Kinetic models for these simulations are given in Fig. 13.

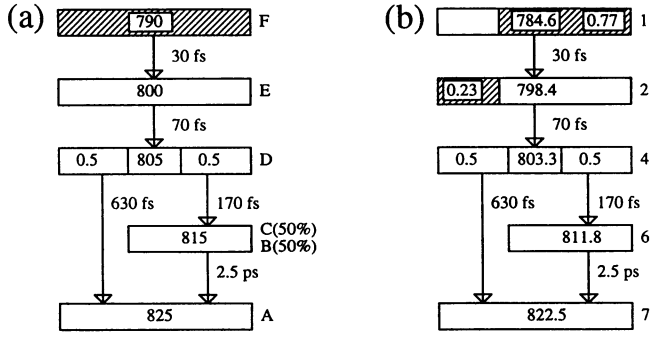

FIGURE 13 Kinetic models for OKT simulations in Fig. 12. (*Left*) In the presence of resonance couplings; (*right*) without resonance couplings. Levels are denoted by level groups *A* through *G* on left, and by pigment numbers 1 through 7 on right. Shading indicates levels excited near 789 nm. This wavelength prepares levels in group *F* in the presence of exciton couplings, whereas it creates a mixture of excitations on pigments 1 and 2 (77% and 23%, respectively) in the absence of couplings.

that absorb near 790 nm (Fig. 7). Sub-100-fs components do not appear in our decay-associated spectra (Fig. 11), because we limited our global analyses to components with longer lifetimes. Our laser cross-correlation function in two-color pump-probe experiments was typically 200–250 fs FWHM; transient hole-burning and/or electronic coherences (Chachisvilis and Sundström, 1996) can influence the kinetics in the region of pulse overlap.

Several variations on the kinetic model in Fig. 13 yield similar OKT surfaces. For example, the effects of varying the proportions of groups *B* and *C* created by energy transfer from group *D* are minor, because the absorption difference spectra for groups *B* and *C* are similar (Fig. 7). A scheme in which laser-excited group *F* levels branch within <100 fs into groups *D* and *E* (which then relax into groups *A* and *B* with 630- and 170-fs kinetics, respectively) appears to work equally well. Given our instrument response, the sub-100-fs lifetimes in our model are order-of-magnitude figures at best.

In summary, our absorption difference simulations can readily distinguish between the OKT and PS Hamiltonians (Lu and Pearlstein, 1993). Combined with our experimental absorption difference spectra, they potentially furnish a new and independent criterion for modeling the FMO electronic structure. In the present context, the OKT Hamiltonian clearly provides a better description for the pump-probe spectroscopy of FMO trimers from *Cb. tepidum*. This conclusion does not necessarily extend to FMO trimers from *P. aestuarii*, for which the OKT and PS Hamiltonians were originally developed; this question awaits comparable experimental data on the FMO protein from the latter species.

The proposal that delocalized exciton states play a role in antenna energy transfer dates back more than 30 years (Robinson, 1964), but their real-time observation remains a current issue. Our experimental and simulated absorption difference spectra unequivocally reflect the presence of strong exciton couplings (like the steady-state absorption and CD spectra; cf. Figs. 6–8 and 10). However, they do not of themselves prove that exciton coherence is maintained during the experimental time scales, because the effects of exciton localization on the absorption difference spectra are subtle and depend on the unknown diagonal energies (cf. *lower right-hand panel* of Fig. 6). The subtlety arises partly because the ESA transitions terminate in delocalized two-exciton states, regardless of the extent of coherence in the probed one-exciton states themselves. Assessing the extent of exciton localization via ordinary absorption difference spectroscopy of FMO trimers will likely require a knowledge of the effective BChl *a* diagonal energies and interactions, to a precision that is as yet unheard of. New strategies for determining the antenna electronic structure (e.g., by independent nonlinear optical techniques) would be valuable.

Herbert van Amerongen made seminal contributions to the early stages of this work.

The Ames Laboratory is operated for the U.S. Department of Energy by Iowa State University under contract no. W-7405-Eng-82. This work was supported by the Division of Chemical Sciences, Office of Basic Energy Sciences.

REFERENCES

Becker, M., V. Nagarajan, and W. W. Parson. 1991. Properties of the excited-singlet states of bacteriochlorophyll *a* and bacteriopheophytin *a* in polar solvents. *J. Am. Chem. Soc.* 113:6840–6848.

Bittner, T., K. D. Irrgang, G. Renger, and M. R. Wasielewski. 1994. Ultrafast excitation energy transfer and exciton-exciton annihilation processes in isolated light-harvesting complexes of photosystem II (LHC II) from spinach. *J. Phys. Chem.* 98:11821–11826.

Blankenship, R. E., P. Cheng, T. P. Causgrove, D. C. Brune, S. H.-H. Wang, J.-U. Choh, and J. Wang. 1993. *Photochem. Photobiol.* 57: 103–107.

Chachisvilis, M., T. Pullerits, M. R. Jones, C. N. Hunter, and V. Sundström. 1994. Coherent nuclear motions and exciton-state dynamics in photosynthetic light-harvesting pigments. *In* Ultrafast Phenomena IX: Proceedings of the 9th International Conference, Dana Point, CA, May 2–6, 1994. P. F. Barbara, W. H. Knox, G. A. Mourou, and A. H. Zewail, editors. Springer-Verlag, Berlin. 435–436.

Chachisvilis, M., and V. Sundström. 1996. The tunnelling contributions to optical coherence in femtosecond pump-probe spectroscopy of the three level system. *J. Chem. Phys.* 104:5734–5744.

Förster, T. 1948. Intermolecular energy transfer and fluorescence. *Ann. Phys. (Leipzig).* 2:55–75.

Freiberg, A., S. Lin, W. Zhou, and R. E. Blankenship. 1996. Ultrafast relaxation of excitons in the bacteriochlorophyll antenna proteins from green photosynthetic bacteria. *In* Ultrafast Processes in Spectroscopy. O. Svelto, S. De Silvestri, and G. Denardo, editors. Plenum Press, New York.

Johnson, S. G., and G. J. Small. 1991. Excited state structure and energy transfer dynamics of the bacteriochlorophyll *a* antenna complex from *Prosthecochloris aestuarii*. *J. Phys. Chem.* 95:471–479.

Knox, R. S. 1975. Excitation energy transfer and migration: Theoretical considerations. *In* Bioenergetics of Photosynthesis. Govindjee, editor. Academic Press, New York. 183–221.

Landau, L. D., and E. M. Lifschitz. 1958. Quantum Mechanics. Pergamon Press, Oxford.

Lin, S., H. C. Chiou, F. A. M. Kleinherenbrink, and R. E. Blankenship. 1994. Time-resolved spectroscopy of energy and electron transfer processes in the photosynthetic bacterium *Heliobacillus mobilis*. *Biophys. J.* 66:437.

Lin, S., H. van Amerongen, and W. S. Struve. 1991. Ultrafast pump-probe spectroscopy of bacteriochlorophyll *c* antennae in bacteriochlorophyll *a*-containing chlorosomes from the green photosynthetic bacterium *Chloroflexus aurantiacus. Biochim. Biophys. Acta.* 1060:13–24.

Lu, X., and R. M. Pearlstein. 1993. Simulations of *Prosthecochloris* bacteriochlorophyll *a* protein optical spectra improved by parametric computer search. *Photochem. Photobiol.* 57:86–91.

Margenau, H., and G. M. Murphy. 1956. The Mathematics of Physics and Chemistry, 2nd Ed. Van Nostrand, New York.

Matthews, B. W., and R. E. Fenna. 1980. Structure of a green bacteriochlorophyll protein. *Acc. Chem. Res.* 13:309–317.

Olson, J. M. 1980. Bacteriochlorophyll *a* proteins of two green photosynthetic bacteria. *Methods Enzymol.* 69:336–344.

Olson, J. M., B. Ke, and K. H. Thompson. 1976. Exciton interactions among chlorophyll molecules in bacteriochlorophyll *a* proteins and bacteriochlorophyll *a* reaction center complexes from green bacteria. *Biochim. Biophys. Acta.* 430:524–537.

Pearlstein, R. M. 1992. Theory of the optical spectra of the bacteriochlorophyll *a* antenna protein trimer from *Prosthecochloris aestuarii. Photosynth. Res.* 31:213–226.

Pearlstein, R. M., and R. P. Hemenger. 1978. Bacteriochlorophyll electronic transition moment directions in bacteriochlorophyll *a* protein. *Proc. Natl. Acad. Sci. USA.* 75:4920–4924.

Philipson, K. D., and K. Sauer. 1972. Exciton interaction in a bacteriochlorophyll protein from *Chloropseudomonas ethylica*. Absorption and circular dichroism at 77 K. *Biochemistry.* 11:1880–1885.

Rahman, T. S., R. S. Knox, and V. M. Kenkre. 1979. Theory of depolarization of fluorescence in molecular pairs. *Chem. Phys.* 44:197–211.

Reddy, N. R. S., R. Jankowiak, and G. J. Small. 1995. High-pressure hole-burning studies of the bacteriochlorophyll *a* antenna complex from *Chlorobium tepidum. J. Phys. Chem.* 99:16168–16178.

Robinson, G. W. 1964. Quantum processes in photosynthesis. *Annu. Rev. Phys. Chem.* 15:311–348.

Savikhin, S. 1995. Shot-noise-limited detection of absorbance changes induced by subpicojoule laser pulses in optical pump-probe experiments. *Rev. Sci. Instrum.* 66:4470–4474.

Savikhin, S., and W. S. Struve. 1994. Ultrafast energy transfer in FMO trimers from the green bacterium *Chlorobium tepidum. Biochemistry.* 33:11200–11208.

Savikhin, S., Y. Zhu, S. Lin, R. E. Blankenship, and W. S. Struve. 1994. *J. Phys. Chem.* 98:10322–10334

Spano, F. C., and S. Mukamel. 1989. Superradiance in molecular aggregates. *J. Chem. Phys.* 91:683–700.

Tronrud, D. E., M. F. Schmid, and B. W. Matthews. 1986. Structure and x-ray amino acid sequence of a bacteriochlorophyll *a* protein from *Prosthecochloris aestuarii* refined at 1.9 Å resolution. *J. Mol. Biol.* 188:443–454.

van Amerongen, H., and W. S. Struve. 1991. Excited state absorption in bacteriochlorophyll *a* protein from the green photosynthetic bacterium *Prosthecochloris aestuarii*: reinterpretation of the absorption difference spectrum. *J. Phys. Chem.* 95:9020–9023.

van Grondelle, R. 1984. Excitation energy transfer, trapping, and annihilation in photosynthetic systems. *Biochim. Biophys. Acta.* 811:147–195.

van Mourik, F., R. R. Verwijst, J. M. Mulder, and R. van Grondelle. 1994. Singlet-triplet spectroscopy of the light-harvesting BChl *a* complex of *Prosthecochloris aestuarii*. The nature of the low-energy 825 nm transition. *J. Phys. Chem.* 98:10307–10312.

Weiss, C. 1972. The pi electron structure and absorption spectra of chlorophylls in solution. *J. Mol. Spectrosc.* 44:37–80.